

Manuscript version: Published Version

The version presented in WRAP is the published version (Version of Record).

Persistent WRAP URL:

<http://wrap.warwick.ac.uk/165011>

How to cite:

The repository item page linked to above, will contain details on accessing citation guidance from the publisher.

Copyright and reuse:

The Warwick Research Archive Portal (WRAP) makes this work by researchers of the University of Warwick available open access under the following conditions.

Copyright © and all moral rights to the version of the paper presented here belong to the individual author(s) and/or other copyright owners. To the extent reasonable and practicable the material made available in WRAP has been checked for eligibility before being made available.

Copies of full items can be used for personal research or study, educational, or not-for-profit purposes without prior permission or charge. Provided that the authors, title and full bibliographic details are credited, a hyperlink and/or URL is given for the original metadata page and the content is not changed in any way.

Publisher's statement:

Please refer to the repository item page, publisher's statement section, for further information.

For more information, please contact the WRAP Team at: wrap@warwick.ac.uk

Quantum Statistical Transport Phenomena in Memristive Computing Architectures

Christopher N. Singh^{1,2}, Brian A. Crafton,³ Mathew P. West,³ Alex S. Weidenbach,³ Keith T. Butler⁴, Allan H. MacDonald,⁵ Arjit Raychowdury,³ Eric M. Vogel,³ W. Alan Doolittle,³ L.F.J. Piper^{1,6} and Wei-Cheng Lee^{1,*}

¹*Department of Physics, Applied Physics, and Astronomy, Binghamton University, Binghamton, New York 13902, USA*


²*Materials Science and Technology Division, Los Alamos National Laboratory, Los Alamos, New Mexico 87545, USA*

³*Department of Electrical and Computer Engineering, Georgia Institute of Technology, Atlanta, Georgia 30332, USA*

⁴*SciML, Scientific Computing Department, Rutherford Appleton Laboratory, Didcot OX110QX, United Kingdom*

⁵*Department of Physics, University of Texas at Austin, Austin, Texas 78712-1081, USA*

⁶*WMG, University of Warwick, Coventry CV4 7AL, United Kingdom*

 (Received 31 August 2020; revised 8 April 2021; accepted 9 April 2021; published 14 May 2021)

The advent of reliable nanoscale memristive components is promising for next-generation compute-in-memory paradigms; however, the intrinsic variability in these devices has prevented widespread adoption. Here, we show coherent electron wave functions play a pivotal role in the nanoscale transport properties of these emerging nonvolatile memories. By characterizing both filamentary and nonfilamentary memristive devices as disordered Anderson systems, the switching characteristics and intrinsic variability arise directly from the universality of electron transport in disordered media. Our framework suggests that localization phenomena in nanoscale solid-state memristive systems are directly linked to circuit-level performance. We discuss how quantum conductance fluctuations in the active layer set a lower bound on device variability. This finding implies that there is a fundamental quantum limit on the reliability of memristive devices and that electron coherence will play a decisive role in surpassing or maintaining Moore's law with these systems.

DOI: [10.1103/PhysRevApplied.15.054030](https://doi.org/10.1103/PhysRevApplied.15.054030)

I. INTRODUCTION

The von Neumann model of computing is the foundation of modern digital technologies but this paradigm harbors an intrinsic bottleneck. This bottleneck arises because data cannot be operated on in the same place that they are stored and, therefore, the computation speed is limited by the rate at which data can be transferred between memory and compute locations [1]. Because of this, solid-state biomimetic computing that avoids this inefficient data transfer and enables a “compute-in-memory” paradigm is highly desired [2]. However, mimicking biological systems that typically have billions of neurons [3] suggests that a solid-state analog would require a similar number of logical units. With transistors already hitting the quantum limits of performance [4], a different class of nanoscale solid-state components is needed and adaptive-oxide memristors are considered among the most promising candidates [5,6]. Although viable solid-state memristors have

already been reported [7], the variability inherent in their operation has been severely detrimental to circuit-level performance [8]. What is more, their underlying switching mechanisms have been hotly debated [9–12].

In solid-state devices, the migration of atomic defects is generally considered sufficient for memristive switching [13] but whether it is necessary—or even optimal—is unclear [14], as purely electronic switching mechanisms have also been proposed [10,15]. In either case, quantum transport effects such as strong electronic correlations, interface scattering, tunneling, and interference may all additionally contribute to the total transport characteristics. Thus, to improve the performance of nanoscale, compute-in-memory devices, a quantum theoretical framework is necessary. This is especially pressing given that the prediction of device properties post fabrication remains the single greatest challenge to widespread adoption [16,17]. The treatment of all the relevant variables in a nonequilibrium quantum framework will therefore accelerate the development pipeline of memristive materials [18].

*wlee@binghamton.edu

This work attempts to fill that gap in the microscopic description of memristive transport by developing a computationally tractable first-principles approach to predict the transport properties of electrons in environments with stochastic disorder potentials. We apply it to filamentary (α -HfO_x) and nonfilamentary (α -Nb₂O_{5-x}) systems. In filamentary devices, we find that electron-phase effects are a significant contributor to variability. In nonfilamentary systems, we find that dynamic disorder potentials can give rise to hysteretic conductance curves. Together, these results indicate that electron-phase effects can significantly influence the performance of compute-in-memory devices. The stochastic nature of the conductance in filamentary systems [19] is shown to be analogous to that of quantum wires near an Anderson localization transition [20]. One of the most astounding properties of quantum disordered systems is that the logarithm of the conductance, not the resistance, stabilizes in the thermodynamic limit [21]. In this way, the conductance becomes a key circuit-level design element because near an Anderson transition, the resistance is not self-averaging. This immediately suggests that interference phenomena could play a central role in the rational design of biomimetic hardware. We anticipate that an understanding of the origin of variability will enable circuit engineers to design more robust compute-in-memory architectures.

II. OVERVIEW OF COMPUTE-IN-MEMORY ARCHITECTURE

Modern computing methods in general, but deep-learning techniques especially, contain a workload of almost entirely matrix multiplication ($\vec{y} = W\vec{x}$) [22]. Neuromorphic hardware is poised to perform this much more efficiently. In traditional von Neumann machines, both the feature data \vec{x} and the matrix weights W_{ij} are transported from main memory to the compute units, where the multiply-and-accumulate (MAC) operations are performed, after which the result \vec{y} is transported and written back into main memory. In this procedure, the energy cost of reading and transporting data from memory to logic greatly outweighs the cost of the MAC [23,24], thus motivating in-memory computing.

A compute-in-memory paradigm performs the MAC operations in a crossbar structure using Ohm's law and a nonvolatile conductance state. This is often known as resistive random access memory (RRAM) [25] but there are other memories that behave similarly. A circuit-level to atomic level schematic of the typical (HfO_x) RRAM is given in Figs. 1(a)–1(c). Each element of the matrix W_{ij} is programmed as a conductance in the crossbar [Fig. 1(a)] and each value of the vector x_i is converted to voltage. The conductance of the active layer [Fig. 1(b)], tuned with external bias, is ultimately set by controlling the electric

potential cross section seen by the electrons. These electrons carry currents along the filaments formed by mobile oxygen vacancies in disordered HfO_x [26], as shown in Fig. 1(c). By Ohm's law, the current through each RRAM device is proportional to the product of the programmed conductance W_{ij} and the applied voltage \vec{x}_i . By Kirchhoff's current law, the resulting currents summed along the columns of the crossbar are proportional to the product of the matrix and vector, \vec{y} . Using this architecture, the only data transport required is the feature vector \vec{x} and result \vec{y} , whereas a typical von Neumann architecture would move \vec{x} and W_{ij} . Assuming that \vec{x} and W_{ij} have the same dimension d , moving only \vec{x} and \vec{y} amounts to a significant saving of $d(d - 1)$ elements.

Although compute-in-memory using the crossbar architecture can greatly reduce data transport, it faces its own limitations at the device level and the circuit level. The two limitations are (1) the number of states the circuit can read at once and (2) the number of distinguishable states that can be accurately read from a column of the crossbar. To read states from the crossbar, an analog-to-digital converter (ADC) converts the analog-current value from the crossbar to a digital value. In Fig. 1(a), the end of each column feeds into an ADC. Modern ADCs are the result of decades of research and can be used to read thousands of states at relatively high speed [27]. However, device variance limits the number of distinguishable states that can be accurately read. Figure 1(d) shows that HfO_x RRAM stacks do have significant variance. It shows that both the measured and predicted dimensionless conductance ($g = G/G_0$) of electroformed HfO_x devices are distributed log-normally. We expand in Sec. V on the details of the quantum framework that enable this prediction but, at this point, it is sufficient to say that this is a quantitative model that also explains the origin of the variability in these devices.

A log-normally distributed conductance means that problem (2) (clearly distinguishing states) is exacerbated, as a large proportion of the available states lie close to each other in value. In Fig. 1(e), we plot the cumulative distribution function for the total conductance resulting from four (left) and eight (right) devices. This figure demonstrates that given enough variance, the current summed along a column will result in an error with a probability given by the distribution of the variance of each device. In this circuit simulation, we use a conductance ratio on a par with experiment [see Fig. 1(d)] and sweep 5%, 10%, and 20% variance. In both cases, 10% and 20% normalized variance results in erroneous compute-in-memory results. Although this is a simple analysis, it clearly demonstrates that increasing the number of devices read will increase the probability of errors due to accumulated variance and that any intrinsic quantum variability is directly tied to circuit-level performance. Therefore, it is desirable to understand the physical origin of the variance in order to mitigate

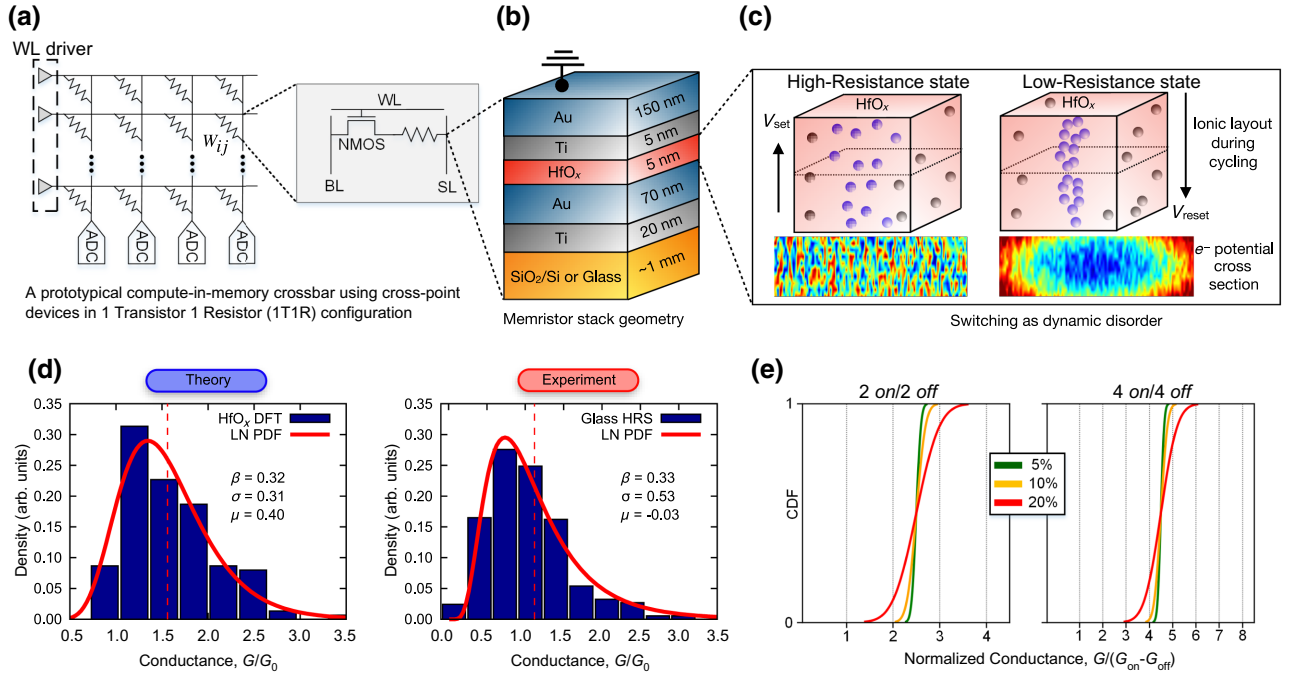


FIG. 1. The relation between device-level variance and circuit-level performance. (a) The circuit-level crossbar architecture with 1-bit word-line drivers and higher-precision ADCs with a NMOS transistor and memristor. In this circuit, the word line (WL) and select line (SL) are set to a high voltage and the resulting current along the bit line (BL) is the result of the read operation. (b) The stack architecture of filamentary memristors set length scale at the device level. (c) A quantum-level description of the mechanism. The set and reset operations generate dynamic potentials for electrons. When the filament is fully formed, a high-transmission-probability path exists. (d) The measured and simulated conductance fluctuations for HfO_x, showing a log-normal character indicative of phase-coherent localization. (e) The effect of variance on the readout performance. The left and right panels show the total normalized conductance of four (left) and eight (right) devices with 5%, 10%, and 20% variance. The black vertical lines represent ADC regions set by conductance difference between on and off state devices ($G_{\text{on}} - G_{\text{off}}$).

it. Before laying out the theory, however, we first establish the well-known conductance properties of filamentary RRAMs.

III. CONDUCTANCE VARIATIONS IN FILAMENTARY DEVICES

The conductance of nanoscale filamentary memristors generally does not follow a normal distribution. Instead, the log of the conductance is distributed normally. This is a general feature of these devices but its origin has been debated [19,28–30]. There are phenomenological models that have considered the statistical properties of the conductance [31] and heuristic models such as trap-assisted tunneling [32] that can recover it, but none *afford it an origin*. In other words, significant effort has been devoted to understanding the log-normal conductance, with the goal of mitigating uncertainty from an engineering perspective, but none of it has considered the possibility that a fundamental quantum limit would manifest. There is, however, this possibility due to the length scales of these devices and the stochastic nature of electron transport in disordered systems.

For example, the many possible configurations of a filament in a thermal environment are one source of conductance fluctuations [33]. In fact, this has been studied quite extensively already, but we do not focus on that in this work. Another source of variability, though, is the many possible paths for electrons to take within any particular filament configuration. Phase-coherence effects between these different electron paths are known to give rise to log-normal conductance fluctuations [21]. To see this schematically, we revisit Fig. 1(c). It depicts a filamentary device in two arbitrary resistance states. In one resistance state, the defects form a filament, while in another resistance state, the defects do not form a continuous filament. In either state, there are many possible defect configurations, each with a different disorder potential for electrons (indicated schematically by the heat maps). As a result, these devices can be considered as dynamically disordered and transport will be heavily influenced by phase coherence and localization effects [34,35]. More importantly, if the transport length L approaches the phase coherence length L_ϕ , the transmission probability for electrons will approach a universal distribution given only by the mean conductance—its character being log-normal

with a normalized variance inversely proportional to its mean [36].

Beyond just a heuristic argument, however, there is additional theoretical and experimental evidence to suggest that quantum effects may play an important role. The evidence mainly takes the form of thermal and dimensional arguments. For example, Basnet *et al.* have shown that thermally insulating substrates can improve the performance of HfO_x stacks by decreasing the variance [37]. Other comprehensive investigations of HfO_x RRAMs have also shown that increasing the temperature of the entire device from 25 °C to 150 °C reduces the log-normal tailing [38]. Beiliard *et al.* have demonstrated that different stack compositions such as $\text{Al}_2\text{O}_3/\text{TiO}_{2-x}$ display an increased variability at cryogenic temperatures [39], suggesting that these effects are not even unique to HfO_x . All these works are commensurate with the idea that increased inelastic scattering at higher temperature could drive $L_\phi \ll L$, restoring uncorrelated diffusive transport and normally distributed conductance. With regard to dimensionality, Bradley *et al.* have shown experimentally that electron injection tends to drive aggregation of oxygen defects into a quasi-one-dimensional (quasi-1D) filament [40,41]. The popular trap-assisted tunneling model [32] sets the current proportional to a barrier-tunneling probability or, equivalently, to the rate of traversing the slowest bridge along a classical percolation path. Therefore, existing theory and experiment both tend to view the transport in nanoscale-filamentary memristors as quasi-1D. In spite of this, existing models are generally semiclassical, even though Funck *et al.* have shown that the quantum behavior might be fundamentally different from semiclassical predictions [42]. Thus, both current theoretical models and experimental evidence suggest that phase-coherence effects can play an important role. Our results indicate that the log-normality of the conductance can, in fact, be attributed to quantum disorder effects and although we use HfO_x as a model system, these results likely apply to other materials systems.

Figure 2 characterizes the conductance variability in our devices. The experimental data are obtained by switching the devices between the low-resistance state (LRS) and the high-resistance state (HRS) multiple times on many devices. To switch to the LRS, a positive voltage sweep is applied to the top electrode, from 0 to 1.2 V. After the device is set to the LRS, a voltage sweep from 0 to 0.1 V is conducted. In postprocessing, the inverse slope of this low-voltage sweep is calculated to determine the resistance of the device. A negative voltage sweep from 0 to -1.5 V is used to reset the device to the HRS. Then, another 0–0.1 V sweep is used to determine the resistance of the HRS. Each device is switched between the LRS and HRS ten times to obtain the cycle-to-cycle variation. This is repeated on 37 devices on a glass substrate and 36 devices on a thin SiO_2/Si substrate. In each panel, a

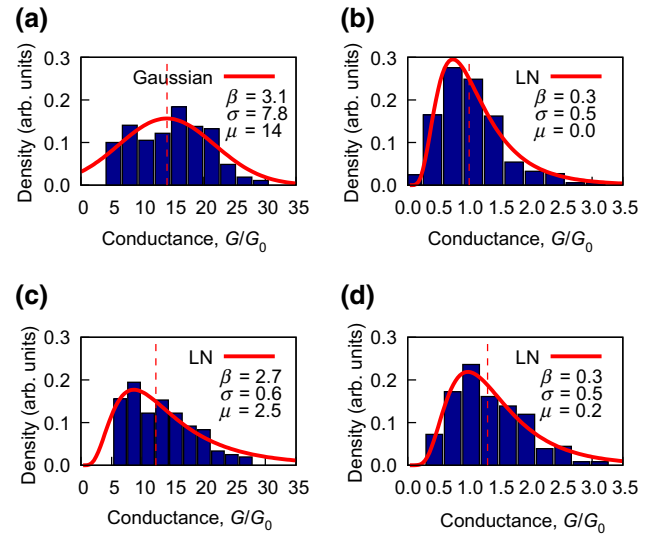


FIG. 2. Experimentally measured distributions of HfO_x memristors. The plot shows conductance distributions on different substrates and in both high- and low-resistance states: (a) glass LRS; (b) glass HRS; (c) silicon LRS; (d) silicon HRS. The data show that over many devices and multiple measurements, a clear statistical distribution emerges that shows log-normal behavior in the conductance, a hallmark of phase-coherent transport.

histogram of conductance measurements is overlaid with either a log-normal or Gaussian distribution, defined as

$$p(g) = \begin{cases} \frac{\beta}{g\sqrt{2\pi\sigma^2}} \exp\left[-\frac{(\ln[g] - \mu)^2}{2\sigma^2}\right], & \text{log-normal,} \\ \frac{\beta}{\sqrt{2\pi\sigma^2}} \exp\left[-\frac{(g - \mu)^2}{2\sigma^2}\right], & \text{Gaussian.} \end{cases}$$

We find that in both the HRS and the LRS with a silicon substrate, the conductance distribution remains log-normal [panels (c) and (d) of Fig. 2]. In the HRS on glass [panel (b) of Fig. 2], we also find log-normal. In the LRS on glass, however [panel (a) of Fig. 2], we find Gaussian or multimodal and attribute this to the difference in thermal conductivity between substrates. These results clearly show that a log-normal conductance manifests experimentally and, furthermore, that it can be altered by reducing the heat flow away from the active layer.

To summarize the filamentary section, our data, along with the generally observed log-normal features of filamentary memristors, as well as the reduction of log-normal tailing with increased temperature, strongly suggest that the origin and behavior of device variance can be described as a quantum wire with dynamic disorder. What this means for filamentary RRAM design is that in addition to variability from stochastic filament dynamics, electron-transport dynamics induce additional variability from interference phenomena. If dominated by electron-phase effects, the conductance variance σ is bounded by

the analytical limit of $\sigma \approx 2/(3\langle g \rangle)$ [36]. This has several meaningful consequences. The first is that to reduce variability and improve RRAM performance, one must reduce L_ϕ to be less than the transport length $L_\phi \ll L$. The second is that the statistical behavior of a single device with many bias-induced random filaments is the same as the statistical behavior of many devices with equally random filaments. This means that ergodic considerations [43] can be taken into account at the circuit-level design, i.e., that device-to-device variance is a manifestation of different disorder distributions and will be distributed in the same way as cycle-to-cycle variance. The third is that the read-to-read variance would be limited by universal conductance fluctuations for cryogenic applications if L_ϕ is larger than the inelastic scattering length. Finally, because the variance of synaptic weights is closely tied to the learning capability of biological and artificial neural networks [44,45], the existence of a quantum source of stochasticity suggests that one could leverage it to mimic the limited precision computation model of biological systems [44].

IV. CONDUCTANCE VARIATIONS IN NONFILAMENTARY SYSTEMS

This section considers the possibility that hysteretic switching in nonfilamentary systems can be equally described within a framework of dynamic disorder. We are motivated by recent advancements demonstrating that Anderson localization can be leveraged as a mechanism of purely electronic switching in silicon [35] and by amorphous, electroforming-free, niobium oxide memdiodes recently developed by Shank *et al.* [46]. We use α -Nb₂O_{5-x} as a model system to test this hypothesis. The first notable difference between filamentary and nonfilamentary systems is that, by definition, nonfilamentary transport cannot be assumed to be quasi-1D. Therefore, the way in which quantum conductance variations present themselves could be totally different. In addition, disorder dynamics are known to be different in the crystalline phase and the amorphous phase [47], so this can have an effect too. In fact, the introduction of disorder can increase the ionic conductivity by up to 4 orders of magnitude in some materials [48,49]. Considering this, and the unique propensity of the niobium oxide series to accommodate dynamic defects [50–52], it is reasonable to assume that disorder potentials will evolve in three dimensions under high field. By extension, if the potential felt by electrons in the presence of a changing ionic environment is dynamic, it is possible that there can be multiple electron transmission probabilities at a given bias. In this way, dynamic disorder allows a unified description of filamentary HfO_x and nonfilamentary α -Nb₂O_{5-x}—the main difference being the dimensionality of transport. We show in Sec. V, however, that the dimensionality is inherently encoded in the matrix elements of

the velocity operator, so that a single framework can treat both cases.

The nonfilamentary devices studied here are annular Ni/ α -Nb₂O_{5-x}/Ni memdiode stacks fabricated on Al₂O₃ substrates. They are 300 nm thick, with a radius of 100 μ m. The normalized conductance in the high-resistance state is approximately 100 times smaller than HfO_x, suggesting stronger localization and three-dimensional (3D) transport. By contrast, the transport direction in the HfO_x RRAMs is approximately 5 nm and the transverse direction is subnanometer, leading to quasi-1D transport. Two different memdiode devices are fabricated and tested. A positive voltage sweep from 0 to 3 V is applied to the top electrode of each device and the subsequent current generated is measured. This voltage sweep is repeated 100 times, with a 2 s delay in between voltage cycles.

Figure 3 summarizes the experimental and theoretical results pertaining to nonfilamentary devices. Panel (a) gives the first-principles electronic structure of the α -Nb₂O_{5-x} active layer of the memdiode. The computational details are given in the Supplemental Material [53]. Panels (b) and (c) show the theoretical and experimental transport characteristics, respectively. In panel (a), oxygen deficiency draws out the conduction band and shifts the chemical potential to a region of finite density of states. Traditionally, this would be an indication of metallic transport but the measurements clearly show diodelike behavior. Therefore, the naive band-theoretical description has already fallen short. If, however, we consider that these states are localized due to disorder, then they would give zero contribution to the conductance until an additional energy is applied to cross the mobility edge. Given that the experimental turn-on voltage is near 2 V [Fig. 3(c)], the localization picture seems more appropriate than the band picture. Panel (b) of Fig. 3 shows the simulated conductance as a function of the energy [54]. The different data points represent conductance values parametrized by different normalized defect velocities v/v_f (effectively, how much of the active layer is disordered). We provide the complete theoretical details in Sec. V but the main result at this stage is that dynamic disorder gives rise to multiple conductance states at a given energy, even while averaged over several specific realizations of disorder. More concretely, at $E - E_f - 1 = 3$ eV, we find that the conductance is greater with $v = 0.9v_f$ than $v = 0.6v_f$, but the opposite is true at $E - E_f - 1 = 2.5$ eV. This means that an interplay between the density of states and localization of the wave functions is contributing to the final conductance. Actually, wave-function localization plays an important role in defining the critical turn-on voltage (details in Sec. V B). This variation in the conductance at a given energy can also be interpreted as a result of the different disorder dynamics in the forward- and reverse-bias directions. Thus, dynamic disorder is a quantum analog of the dynamic boundary between regions of

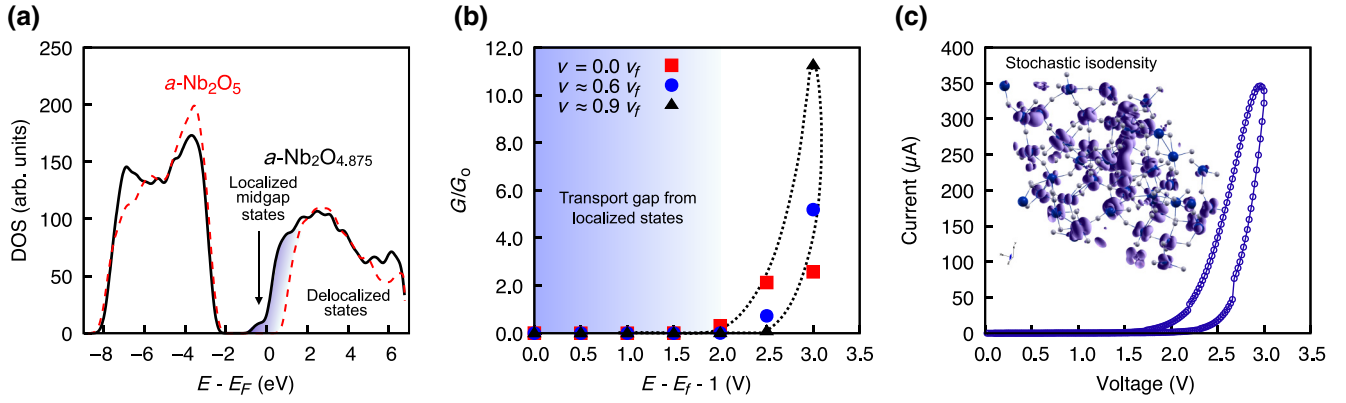


FIG. 3. Mobility edge switching and hysteresis with dynamic disorder. (a) The electronic structure: the density of states for amorphous stoichiometric ($a\text{-Nb}_2\text{O}_5$) and off-stoichiometric ($\text{Nb}_2\text{O}_{4.875}$) niobium oxide. Oxygen deficiency draws out the conduction band and shifts the chemical potential by approximately 1 eV. The shading indicates a region of strong localization and the region integrated to produce the isodensity surface, shown as an inset in part (c) in the rightmost panel. (b) Simulated conductance with dynamic disorder. By assuming a greater vacancy transport (disorder potential redistribution), a single operating bias can have multiple conductance states. Each point is averaged over five disorder realizations with $W = 3$ eV. The dotted line is a guide to the eye. (c) The annular memdiode-device I - V character. The inset shows the $0.1e^-/\text{\AA}^3$ isodensity surface, demonstrating the stochastic landscape for electrons in establishing a current.

high and low dopant concentrations originally envisioned by Strukov *et al.* [13]. Panel (c) gives the measured I - V curve. Comparing the theoretical result in panel (b) and the experimental result in panel (c), the similar features indicate dynamic disorder and localization effects can, in fact, enable memdiodelike I - V behavior.

To summarize the nonfilamentary section, dynamic disorder potentials in 3D manifest conductance variations that are quite different than those in quasi-1D structures. Nevertheless, both can be attributed to electron-phase effects in highly disordered systems. This result suggests that the critical voltage is dictated by localization and that the spread in the hysteresis is related to the dynamic disorder potential. Because the statistical distribution and the I - V characteristics of two very different systems can be reproduced in a single approach, we resolve dynamic disorder as a viable quantum framework to treat memristive switching. Given the evidence presented thus far, we now turn to detailing the theoretical framework and providing a complete theoretical justification for its use in this circumstance.

V. THEORETICAL TREATMENT OF DYNAMIC DISORDER

A. Construction of the Hamiltonian

A quantum treatment begins with the Hamiltonian. We define it as the sum of the kinetic and stochastic components, as

$$H = H_t + H_s + H_h. \quad (1)$$

Here, H_t is the kinetic term, H_s is the substitutional disorder induced by vacancies or replacements, and H_h is the hopping disorder arising from deformation of atomic positions, interstitials, etc. The kinetic term can be expressed as

$$H_t = \frac{1}{2} \sum_{ij\alpha\beta} (t_{ij}^{\alpha\beta} - 2\mu\delta_{ij}\delta_{\alpha\beta}) c_{i\alpha}^\dagger c_{j\beta}. \quad (2)$$

The fermion operators $c_{i\alpha}^\dagger$ create (destroy) particles at site $i(j)$, with orbital and spin character denoted by α (β), and μ denotes the chemical potential. In the limit of $H_s = H_h = 0$, the kinetic integrals $t_{ij}^{\alpha\beta}$ are sufficient to determine the bulk-transport properties of long-range ordered solids. They can be calculated using standard density-functional theory (DFT) techniques and a Fourier transformation into a real-space localized basis [55]. The challenge, however, is that to study the statistical behavior of many disorder configurations, many, expensive, molecular-dynamic simulations of large supercells, followed by density-functional calculations, would be required. It is therefore worthwhile to pursue a cheaper way to model statistical properties, yet retain (to the extent that it is possible) a completely first-principles description of the electronic structure. In this spirit, there are two types of disorder that can be parameterized once H_t is known: diagonal and off-diagonal disorder. Atomic vacancies or substitutions are diagonal elements in the total Hamiltonian and act purely as a local potential, as described by

$$H_s = \sum_{ij\alpha\beta} \Theta_{ij}^{\alpha\beta}(W) \delta_{ij} \delta_{\alpha\beta} c_{i\alpha}^\dagger c_{j\beta}. \quad (3)$$

Deformation of atomic positions or interstitials manifest as off-diagonal modulation of the kinetic energy density. We make the approximation that in the amorphous phase, the atomic positions are randomly perturbed from their equilibrium positions in the ordered state, and this effect is written as

$$H_h = \sum_{ij\alpha\beta} (1 - \delta_{ij} \delta_{\alpha\beta}) \Theta_{ij}^{\alpha\beta}(W) c_{i\alpha}^\dagger c_{j\beta}. \quad (4)$$

The matrix elements $\Theta_{ij}^{\alpha\beta}(W)$ appearing in H_s and H_h are random numbers drawn from a uniform distribution of width W , centered at zero. With this distribution, the chemical potential of the disordered system is the same as that of the clean system. This is not strictly required for our argument but simplifies the analysis.

With the kinetic term H_t taken from first principles, we need only justify the disorder potential ($H_s + H_h$) being physical. We achieve this by performing 20 *ab initio* molecular-dynamic quenches and calculating the distribution of the Hartree potential using DFT. We then set the maximum disorder strength W to be less than the full width at half maximum of this distribution [53]. The advantage of this approach is that we can generate any number of physically justified disorder realizations and gather statistical information on important metrics such as transport coefficients, the mobility edge, and wave-function localization, at far less computational expense than in the traditional approach. To determine the distribution of the conductance in many disordered filaments, this is sufficient. Each filament realizes a random disorder potential. The final part, however, is to incorporate the dynamic aspect of a disorder potential.

To model a dynamic disorder potential in 3D, we make two reasonable assumptions. First, we assume that electrons equilibrate instantaneously compared to ionic time scales. Second, we assume that defects drift in an applied field. This is an approximation, because diffusion and thermophoresis also contribute to defect transport [56,57]. However, this simple approximation allows us to treat dynamic disorder through a spatially dependent probability density. The probability that any given site in the lattice has a defect, P_k , becomes a function of time and applied bias $P_k \rightarrow P_k(V, t)$. In the linear-drift approximation, we can assume that this probability is parametrized at small time values by the drift velocity v . Thus, in the absence of an external field, $v = 0$, and every site in the lattice is equally likely to have a defect. But as the external bias is applied, defects drift and are less likely reside in a region of vt away from (or closer to) an electrode (depending on the defect charge and bias polarity). Motivated by the boundary idea of Strukov *et al.*, we assume $P_k(V, t) = 0$ if the lattice site is in a region of reduced defects, and $P_k(V, t) = 1$ in the other region. In principle, the nature of the probability function can be adapted to include any

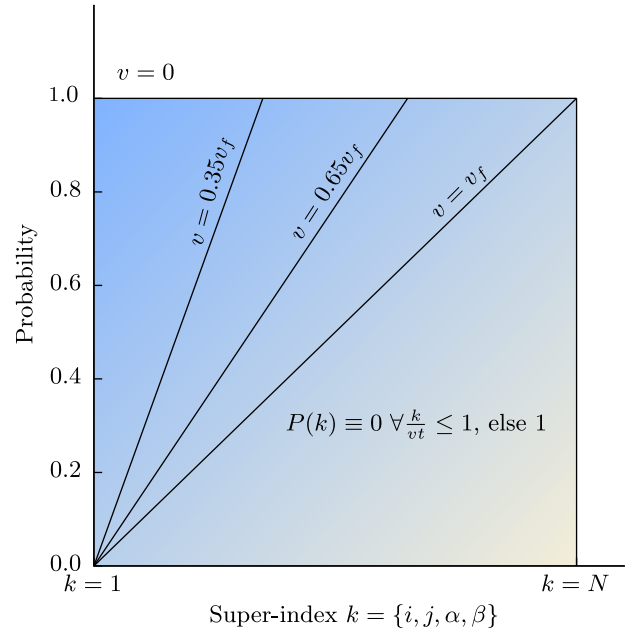


FIG. 4. The characterization of a dynamic distribution of disorder. The plot shows that the probability distribution of having a defect is dependent on the ionic velocity v .

number of effects and if it was exact, then the description would be exact. This approach effectively redefines Eq. (1) to become bias and time dependent. The coupled system-environment Hamiltonian $H(V, t)$ can be written (ignoring H_h) as

$$H(V, t) = H_t + \sum_{ij\alpha\beta} \Theta_{ij}^{\alpha\beta}(W) P_{ij}^{\alpha\beta}(V, t) \delta_{ij} \delta_{\alpha\beta} c_{i\alpha}^\dagger c_{j\beta}. \quad (5)$$

Figure 4 shows the linear probability distribution implemented as a function of the Hamiltonian superindex k (covers site and orbital indices). This is used in simulating the conductance of $a\text{-Nb}_2\text{O}_{5-x}$ [Fig. 3(b)]. The central quantity is the defect velocity v . If $v = 0$, there is no motion of defects and every site is equally likely to have a defect. If $v \neq 0$, then the probability for a site to have a defect changes proportional to v . We calibrate a limiting velocity v_f by the equilibration times for I - V curves in our $a\text{-Nb}_2\text{O}_{5-x}$ devices. For example, if it takes 100 s for the current to stabilize in a 300-nm-thick sample, we may assume that the slowest-moving ions are traveling at 3 nm/s. This is reasonable for good ionic conductors [58]. This defines the shallowest slope of our probability curve ($v = v_f$) but if ions have a lesser propensity to move, we can set the slope to a fraction of v_f .

To implement this approach, one chooses an arbitrary measurement time and a velocity. This defines the disorder potential. Then, the Hamiltonian is constructed, exactly diagonalized, and the wave functions are used to determine the transport coefficients (the linear-response theory details

are in Sec. V B). It is worth mentioning that this approach is *not* a simulation of the ionic motion itself; rather, it enables a quantum statistical description of the memristive transport. The time dynamics of the potential that we have employed here is only an approximation. Nevertheless, by taking a linear one, we have found that the spread in the conductance at a given bias is in line with the experimental result.

B. Transport in the presence of disorder: Validity of Kubo expression

Thus far, we have not established a theoretical approach to determine the transport coefficients in dynamic disorder environments. We use the finite-size implementation of the Kubo conductivity tensor, defined as [59]

$$\sigma_{\alpha\beta}(\mu, T) \equiv \frac{-i\hbar e^2}{N} \sum_{nn'} \frac{\Delta f_{nn'}}{\varepsilon_n - \varepsilon_{n'}} \frac{\langle n | v_\alpha | n' \rangle \langle n' | v_\beta | n \rangle}{\varepsilon_n - \varepsilon_{n'} + i\eta}. \quad (6)$$

In Eq. (6), N is the number of unit cells, $|n\rangle$ is an eigenstate of the total Hamiltonian H with eigenenergy ε_n , v is the velocity operator, and $\Delta f_{nn'}$ represents the occupation difference between the state n and n' . $\Delta f_{nn'}$ carries an implicit dependence on the temperature and chemical potential through the Fermi function. The matrix elements of the velocity operator are defined by Eq. (7), where r_i is the real-space position of state i and \hat{e}_α is the unit vector along direction α :

$$i\hbar v_{ij}^\alpha = (r_i - r_j) \cdot \hat{e}_\alpha H_{ij}. \quad (7)$$

To establish the validity of the finite-size Kubo formula for applications to real material systems near an Anderson transition, we benchmark against model systems with a known localization transition. We choose a one- and two-band nearest-neighbor tight-binding model with cubic symmetry and 1331 unit cells. The single-band Hamiltonian has a known localization transition at $W = 16.5t$ [60] but because we are primarily interested in gapped systems, we also benchmark the two-band model. The dispersion in the one-band case is simply defined as

$$E(k) = -2t[\cos(kx) + \cos(ky) + \cos(kz)]. \quad (8)$$

It is common to set the hopping parameter t in this one-band model to unity. The bandwidth is then $12t$. In the two-band model, there are two on-site degrees of freedom with energy $\pm\epsilon$. In the Hamiltonian, the only nonzero hopping

elements $t_{ij}^{\alpha\beta}$ are defined as

$$\begin{aligned} t_{\alpha,\alpha}^{i=j} &= -\epsilon \\ t_{\alpha,\beta}^{i=j} &= e^{-2|\mathbf{r}_i - \mathbf{r}_j|} \\ t_{\beta,\alpha}^{i=j} &= e^{-2|\mathbf{r}_i - \mathbf{r}_j|} \\ t_{\beta,\beta}^{i=j} &= +\epsilon. \end{aligned} \quad (9)$$

Using these expressions, we can investigate the electronic structure and wave-function localization as a function of disorder W across the transition in known systems and compare that to the DFT result for $\text{Nb}_2\text{O}_{5-x}$. The details for obtaining the DFT result are given in the Supplemental Material [53].

Figure 5 shows the Kubo response as a function of the energy for various strengths of disorder in the various systems overlaid with the density of states. The solid lines show the density of states and the dotted lines show the Kubo conductivity. As expected, we see that the one- and two-band models undergo a transition to a completely transportless phase with increasing disorder strength. This demonstrates that the finite-size Kubo expression is, in fact, capable of capturing Anderson localization. The evidence is that we see a finite density of states, yet zero conductivity inside the Anderson localized phase ($W = 20$). The implications for oxygen-poor $\alpha\text{-Nb}_2\text{O}_{5-x}$ are shown in Fig. 5(c), where at $W = 5$ eV, the highly localized in-gap states give zero contribution to the linear response. The importance of the matrix element effects are readily apparent across all systems, because the finite density of states across the chemical potential means that the occupation factor $\Delta f_{nn'}/(\varepsilon_n - \varepsilon_{n'})$ in the Kubo expression is positive but the phase coherence forms a transport gap. This is only possible if the velocity matrix elements go to zero. This analysis shows that for pairs of wave functions with similar thermal occupation, or small eigenstate coupling, the contribution to the finite-size Kubo conductivity will be small and that interference effects are captured by the matrix elements of the velocity operator. Because the time scale for the ionic drift is usually much slower than that of the electronic response, the electronic structure will be established immediately after the oxygen vacancies reach new locations. Given these pieces of evidence, the Kubo formula is a valid approach to compute the conductivity at each snapshot in time.

C. Characterization of localized wave functions

To determine if the midgap states contribute to transport in the presence of localization effects, we handcraft a metric of localization focused on transport. In some sense, it is analogous to the well-known inverse participation ratio [61] but considers not only the wave-function extent but also virtual coupling of all states in the system. To do so,

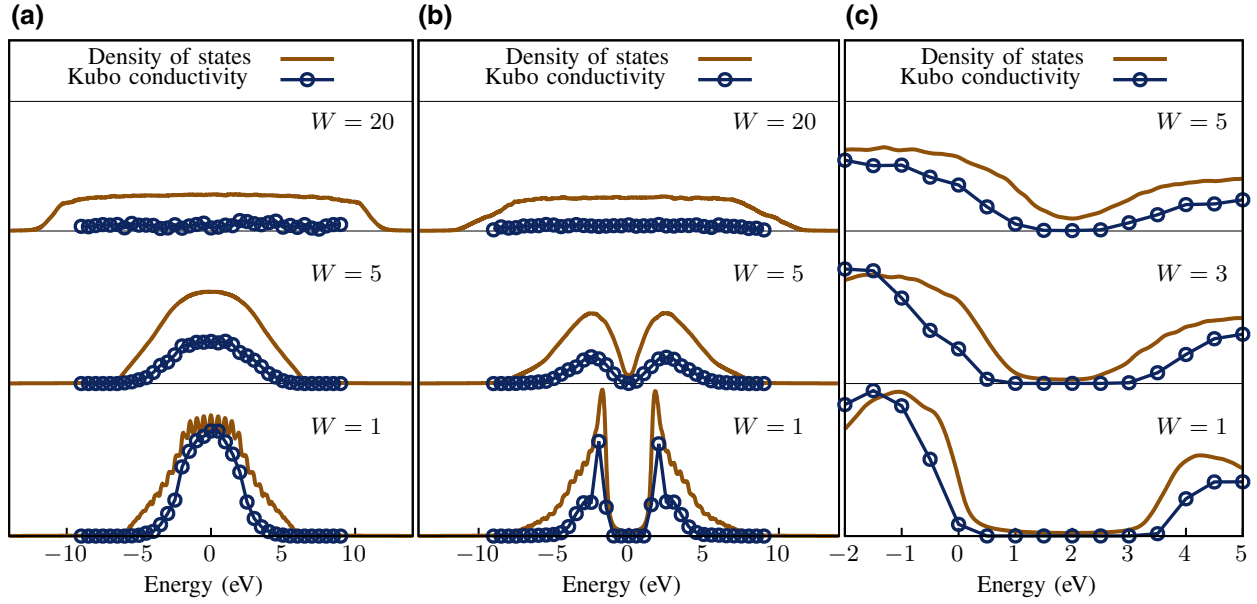


FIG. 5. The quantification of the in-gap contribution to the conductivity. The dotted lines plot the finite-size Kubo conductivity as a function of the energy at 300 K in (a) a single-band model, (b) the two-band model, and (c) the first-principles DFT Nb_2O_5 . The solid lines show the density of states on the same dependent axis with a globally arbitrary, but internally relative, vertical scale.

we first define the object ϕ^{mn} as

$$\phi^{mn} = \sum_r |\langle m|r \rangle \langle r|n \rangle|^2. \quad (10)$$

If $\{|n\rangle\}$ and $\{|m\rangle\}$ represent eigenvectors of the total Hamiltonian H in Eq. (1), then Eq. (10) can be interpreted as a collection of the probabilities for states to couple through the eigenspace. We would like to characterize the dispersion of ϕ^{mn} , so we can define the Gini coefficient [62] of the n th eigenstate with energy ε_n as

$$g(\varepsilon) = \sum_n \chi^n \delta(\varepsilon - \varepsilon_n), \quad (11)$$

where

$$\chi^n \equiv [2N \sum_m \phi^{mn}]^{-1} \sum_{mm'} |\phi^{mn} - \phi^{m'n}|. \quad (12)$$

In this formulation, $g \in [0, 1]$, and will describe the distribution of the propensity of an electron to change state. If this state is characterized by $g = 0$, then it has equal propensity to transition to any other state in the system. This is not the case in real systems, so in practice the Gini coefficient of active states lies in the middle of the measure. On the other hand, if $g = 1$, the state cannot transition to any other state and this is a physically realizable situation by many mechanisms. Therefore, states with a Gini coefficient of one will effectively be silent, as they do not couple through the eigenspace to any other state. This approach

may prove to generalize beyond the inverse participation ratio in characterizing transport properties because there are many transport mechanisms facilitated by spatially local wave functions [63]. While we only consider electronically coupled states here, in principle this could be extended to include states coupled by other mediators; for example, phonons in variable-range hopping situations. When connected to *ab initio* simulations of disordered systems, this is a simple yet powerful method to gauge the mobility edge in real materials.

The density of states and the Gini coefficient as a function of disorder are shown in the panels of Fig. 6. The density of states is shown by the solid lines and the Gini coefficient by the points. In all three panels, the abscissa is absolute and physical. The ordinate for the Gini coefficient is absolute but the ordinate for the density of states is only internally relative and arbitrary. Panel (a) shows the single-band model, panel (b) the two-band model, and panel (c) the DFT result for Nb_2O_5 . The single- and two-band models shown in Fig. 6 are again used as a benchmark. For zero disorder, the Gini coefficient is uniform and the insulating gap is clearly visible. As the disorder is increased to $W = 3$, the Gini coefficient spikes for states near the chemical potential, then quickly decays at higher energy. This demonstrates that, in principle, we can resolve a mobility edge. Fig. 6(c) shows the first-principles result for Nb_2O_5 . At $W = 0$ eV, there is an insulating gap in the density of states and the Gini coefficient. As the disorder is increased to $W = 3$ eV, the gap begins to close but remains finite and the Gini coefficient of the in-gap states spikes. At $W = 5$ eV, states completely span the gap.

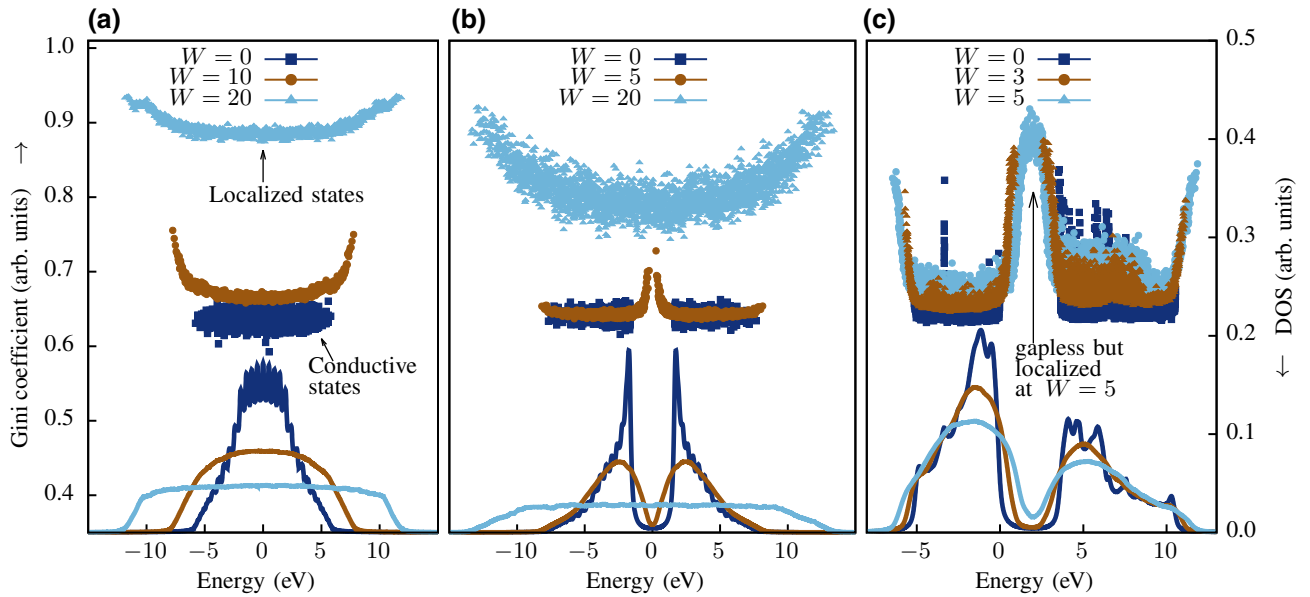


FIG. 6. Modeling the population of in-gap states and their localization. The lines plot the density of states as a function of disorder strength W and the dots represent the Gini coefficient: (a) a single-band model; (b) **HERE** an arbitrarily gapped two-band model; (c) the density-functional result for a 50-band 197-unit supercell of Nb_2O_5 . W specifies the width of the box distribution in electronvolts.

In clean systems, this would be an indication of metallic behavior. However, the extent to which states inside the gap couple to all other states is greatly reduced, indicated by a tendency of the Gini coefficient toward unity. This situation greatly reduces the number of conducting channels available and indicates phase-coherent localization of these midgap states.

To summarize the theoretical section, development of the dynamic disorder potential, a viable implementation of the linear response, and a metric of localization represents a framework to understand quantum statistical effects in memristive computing architectures. Predictions in filamentary and nonfilamentary systems are presented in Figs. 1–3—they compare well with experiment. Figures 6 and 5 demonstrate that we can resolve localized wave functions in our approach and that the Kubo formula is a viable tool to model the linear response. One framework gives a quantum statistical origin to the log-normal conductance fluctuations in filamentary RRAMs and enables quantitative predictions. It also exposes the role of localization in the critical voltage and hysteresis in nonfilamentary systems. With this in mind, we now discuss the general implications of this framework for in-memory computing.

VI. GENERAL IMPACT FOR COMPUTE-IN-MEMORY ARCHITECTURES

With the evidence presented thus far, some rather general and striking aspects of the agency of neuromorphics to transcend Moore’s law emerge. These general aspects originate in the behavior of nanoscale memristors. They are as follows:

1. The basic quantum properties of disordered systems at the nanoscale are an *immutable* source of variability.
2. The ergodic hypothesis ensures that device-to-device variability is the same as cycle-to-cycle variability, as each are just different instantiations of disorder.
3. The logarithm of the conductance, not the resistance, obeys the central-limit theorem.

So while the classical conception of neuromorphics is to accelerate matrix operations using a *well-defined* state, there is an additional and possibly more important ability of a truly neuromorphic system; that is, the ability to fall into nondeterministic states. Any machine, no matter how complex or multivariate, can hardly be considered intelligent if its products, possibly *ad infinitum*, are yet deterministic.

Therefore, the promise of neuromorphics lies not only in the ability to circumvent the von Neumann bottleneck but also in the ability to leverage quantum nondeterminism for truly intelligent hardware designs. Future efforts can now be directed toward learning algorithms incorporating the statistical nature of logical nodes. For example, one may envision a simple neural network where the state of each node is not known precisely but, rather, is drawn from a log-normal distribution with a variance inversely proportional to the running average of its activations. This is how the brain itself works [44] and, as such, a machine of this type may have greater generalizability due to the finite probability of each of its nodes to take on values far from their means. In this sense, what has thus far been considered a hindrance is realized as actually being a utility and

is rooted in the quantum transport properties of nanoscale disordered systems.

VII. CONCLUSIONS

We present a unified description of the switching characteristics and intrinsic variability of two very different classes of memristive devices, suggesting design paradigms and connections to the fundamental processes of biomimetic learning. The ability of our framework to reproduce salient experimental signatures shows that quantum interference phenomena are directly linked to circuit-level performance with implications for the endurance, reliability, and scaling of neuromorphic hardware. Although we demonstrate the close relation between oxygen deficiency, disorder, and memristive response in electroforming free a -Nb₂O_{5-x} and filamentary a -HfO_x, the minimal ingredients for this physics can be found in many systems, requiring only dynamic disorder. In fact, we suspect that memristive hysteresis should be found in practically all disordered systems as long as there are nearby metastable configurations that can be accessed with an impulse. The understanding gained from circuit realizations of intelligence may even provide insight into the functioning of the human brain.

ACKNOWLEDGMENTS

This work was supported by the Air Force Office of Scientific Research Multidisciplinary Research Initiative (MURI), entitled “Cross-Disciplinary Electronic-Ionic Research Enabling Biologically Realistic Autonomous Learning (CEREBRAL)” under Award No. FA9550-18-1-0024 administered by Dr. Ali Sayir.

C. N. Singh, L. F. J. Piper, and W.-C. Lee conceived the study of the conductance distributions. C. N. Singh designed and performed the theoretical analysis of the conductance fluctuations. K. T. Butler performed the molecular-dynamic simulations. B. A. Crafton and A. Raychowdury conducted the circuit analysis. A. S. Weidenbach and W. Alan Doolittle fabricated and performed the experiments for Nb₂O_{5-x} devices and M. P. West and E. M. Vogel those for HfO_x. C. N. Singh, L. F. J. Piper, A. H. MacDonald, and W.-C. Lee analyzed the experimental data and theoretical simulations. C. N. Singh, L. F. J. Piper, and W.-C. Lee wrote the manuscript, with inputs from all authors. C. N. Singh, L. F. J. Piper, and W.-C. Lee ensured the clarity of the manuscript.

The authors declare no competing interests.

-
- [1] F. Williams and T. Kilburn, Electronic digital computers, *Nature* **162**, 487 (1948).
 - [2] V. K. Sangwan and M. C. Hersam, Neuromorphic nanoelectronic materials, *Nat. Nanotechnol.* **15**, 517 (2020).

- [3] G. Indiveri, B. Linares-Barranco, R. Legenstein, G. Deligeorgis, and T. Prodromakis, Integration of nanoscale memristor synapses in neuromorphic computing architectures, *Nanotechnology* **24**, 384010 (2013).
- [4] J. R. Powell, The quantum limit to Moore’s law, *Proc. IEEE* **96**, 1247 (2008).
- [5] R. Waser, H. Keller, and U. Erb, In *Nanoelectronics and Information Technology: Advanced Electronic Materials and Novel Devices*, edited by R. Waser (Wiley-VCH GmbH & Co. KGaA, Weinheim, 2003).
- [6] J. J. Yang, M. D. Pickett, X. Li, D. A. Ohlberg, D. R. Stewart, and R. S. Williams, Memristive switching mechanism for metal/oxide/metal nanodevices, *Nat. Nanotechnol.* **3**, 429 (2008).
- [7] J. Zhu, T. Zhang, Y. Yang, and R. Huang, A comprehensive review on emerging artificial neuromorphic devices, *Appl. Phys. Rev.* **7**, 011312 (2020).
- [8] J. J. Yang, F. Miao, M. D. Pickett, D. A. Ohlberg, D. R. Stewart, C. N. Lau, and R. S. Williams, The mechanism of electroforming of metal oxide memristive switches, *Nanotechnology* **20**, 215201 (2009).
- [9] W. Sun, B. Gao, M. Chi, Q. Xia, J. J. Yang, H. Qian, and H. Wu, Understanding memristive switching via *in situ* characterization and device modeling, *Nat. Commun.* **10**, 1 (2019).
- [10] M. D. Pickett, G. Medeiros-Ribeiro, and R. S. Williams, A scalable neuristor built with Mott memristors, *Nat. Mater.* **12**, 114 (2013).
- [11] J. del Valle, Y. Kalcheim, J. Trastoy, A. Charnukha, D. N. Basov, and I. K. Schuller, Electrically Induced Multiple Metal-Insulator Transitions in Oxide Nanodevices, *Phys. Rev. Appl.* **8**, 054041 (2017).
- [12] R. Waser, R. Dittmann, G. Staikov, and K. Szot, Redox-based resistive switching memories—nanoionic mechanisms, prospects, and challenges, *Adv. Mater.* **21**, 2632 (2009).
- [13] D. B. Strukov, G. S. Snider, D. R. Stewart, and R. S. Williams, The missing memristor found, *Nature* **453**, 80 (2008).
- [14] H. Wang and X. Yan, Overview of resistive random access memory (RRAM): Materials, filament mechanisms, performance optimization, and prospects, *Phys. Status Solidi RRL* **13**, 1900073 (2019).
- [15] J. del Valle, P. Salev, Y. Kalcheim, and I. K. Schuller, A caloritronics-based Mott neuristor, *Sci. Rep.* **10**, 1 (2020).
- [16] G. Molas, G. Sassine, C. Nail, D. A. Robayo, J.-F. Nodin, C. Cagli, J. Coignus, P. Blaise, and E. Nowak, Resistive memories (RRAM) variability: Challenges and solutions, *ECS Trans.* **86**, 35 (2018).
- [17] X. Lian, X. Shen, L. Lu, N. He, X. Wan, S. Samanta, and Y. Tong, Resistance switching statistics and mechanisms of Pt dispersed silicon oxide-based memristors, *Micromachines* **10**, 369 (2019).
- [18] D. Panda, P. P. Sahu, and T. Y. Tseng, A collective study on modeling and simulation of resistive random access memory, *Nanoscale Res. Lett.* **13**, 8 (2018).
- [19] W. Yi, S. E. Savel’Ev, G. Medeiros-Ribeiro, F. Miao, M.-X. Zhang, J. J. Yang, A. M. Bratkovsky, and R. S. Williams, Quantized conductance coincides with state instability and excess noise in tantalum oxide memristors, *Nat. Commun.* **7**, 1 (2016).

- [20] K. A. Muttalib and P. Wölfle, “One-Sided” Log-Normal Distribution of Conductances for a Disordered Quantum Wire, *Phys. Rev. Lett.* **83**, 3013 (1999).
- [21] A. Abrikosov, The paradox with the static conductivity of a one-dimensional metal, *Solid State Commun.* **37**, 997 (1981).
- [22] V. Sze, Y.-H. Chen, T.-J. Yang, and J. S. Emer, Efficient processing of deep neural networks: A tutorial and survey, *Proc. IEEE* **105**, 2295 (2017).
- [23] M. Horowitz, in *2014 IEEE International Solid-State Circuits Conference Digest of Technical Papers (ISSCC)* (IEEE, 2014), p. 10.
- [24] Y.-H. Chen, T. Krishna, J. S. Emer, and V. Sze, Eyeriss: An energy-efficient reconfigurable accelerator for deep convolutional neural networks, *IEEE J. Solid-State Circuits* **52**, 127 (2017).
- [25] F. Zahoor, T. Z. Azni Zulkifli, and F. A. Khanday, Resistive random access memory (RRAM): An overview of materials, switching mechanism, performance, multilevel cell (MLC) storage, modeling, and applications, *Nanoscale Res. Lett.* **15**, 1 (2020).
- [26] D. Z. Gao, J. Strand, M. S. Munde, and A. L. Shluger, Mechanisms of oxygen vacancy aggregation in SiO_2 and HfO_2 , *Front. Phys.* **7**, 43 (2019).
- [27] R. H. Walden, Analog-to-digital converter survey and analysis, *IEEE J. Sel. Areas Commun.* **17**, 539 (1999).
- [28] J. S. Lee, S. Lee, and T. W. Noh, Resistive switching phenomena: A review of statistical physics approaches, *Appl. Phys. Rev.* **2**, 031303 (2015).
- [29] Y. Li, S. Long, Y. Liu, C. Hu, J. Teng, Q. Liu, H. Lv, J. Suñé, and M. Liu, Conductance quantization in resistive random access memory, *Nanoscale Res. Lett.* **10**, 1 (2015).
- [30] R. Degraeve, A. Fantini, N. Raghavan, L. Goux, S. Clima, Y.-Y. Chen, A. Belmonte, S. Cosemans, B. Govoreanu, D. J. Wouters, *et al.*, in *Proceedings of the 21th International Symposium on the Physical and Failure Analysis of Integrated Circuits (IPFA)* (IEEE, 2014), p. 245.
- [31] V. Karpov and D. Niraula, Log-normal statistics in filamentary RRAM devices and related systems, *IEEE Electron Device Lett.* **38**, 1240 (2017).
- [32] M. P. Houn, Y. H. Wang, and W. J. Chang, Current transport mechanism in trapped oxides: A generalized trap-assisted tunneling model, *J. Appl. Phys.* **86**, 1488 (1999).
- [33] S. Datta, *Electronic Transport in Mesoscopic Systems*, Cambridge Studies in Semiconductor Physics and Microelectronic Engineering (Cambridge University Press, Cambridge, 1995).
- [34] C. Chandrashekar and T. Busch, Quantum percolation and transition point of a directed discrete-time quantum walk, *Sci. Rep.* **4**, 6583 (2014).
- [35] Y. Lu, A. Alvarez, C.-H. Kao, J.-S. Bow, S.-Y. Chen, and I.-W. Chen, An electronic silicon-based memristor with a high switching uniformity, *Nat. Electron.* **2**, 66 (2019).
- [36] T. M. Nieuwenhuizen and M. C. W. van Rossum, Intensity Distributions of Waves Transmitted through a Multiple Scattering Medium, *Phys. Rev. Lett.* **74**, 2674 (1995).
- [37] P. Basnet, D. G. Pahinkar, M. P. West, C. Perini, S. Graham, and E. Vogel, Substrate dependent resistive switching in amorphous- HfO_x memristors: An experimental and computational investigation, *J. Mater. Chem. C* **8**, 5092 (2020).
- [38] A. Fantini, L. Goux, R. Degraeve, D. Wouters, N. Raghavan, G. Kar, A. Belmonte, Y.-Y. Chen, B. Govoreanu, and M. Jurczak, in *2013 5th IEEE International Memory Workshop* (IEEE, 2013), p. 30.
- [39] Y. Beiliard, F. Paquette, F. Brousseau, S. Ecoffey, F. Alibert, and D. Drouin, Investigation of resistive switching and transport mechanisms of $\text{Al}_2\text{O}_3/\text{TiO}_{2-x}$ memristors under cryogenic conditions (1.5 K), *AIP Adv.* **10**, 025305 (2020).
- [40] S. R. Bradley, A. L. Shluger, and G. Bersuker, Electron-Injection-Assisted Generation of Oxygen Vacancies in Monoclinic HfO_2 , *Phys. Rev. Appl.* **4**, 064008 (2015).
- [41] S. R. Bradley, G. Bersuker, and A. L. Shluger, Modelling of oxygen vacancy aggregates in monoclinic HfO_2 : Can they contribute to conductive filament formation? *J. Phys.: Condens. Matter* **27**, 415401 (2015).
- [42] C. Funck, A. Marchewka, C. Bäumer, P. C. Schmidt, P. Müller, R. Dittmann, M. Martin, R. Waser, and S. Menzel, A theoretical and experimental view on the temperature dependence of the electronic conduction through a Schottky barrier in a resistively switching SrTiO_3 -based memory cell, *Adv. Electron. Mater.* **4**, 1800062 (2018).
- [43] The ergodic hypothesis is that after a long enough time, all the microstates of the system with the same energy will be accessed equiprobably. It has been widely employed in the study of disorder effects [73] and is one of the most basic assumptions in equilibrium quantum statistics [74–76].
- [44] G. Buzsáki and K. Mizuseki, The log-dynamic brain: How skewed distributions affect network operations, *Nat. Rev. Neurosci.* **15**, 264 (2014).
- [45] K. Rajan and L. F. Abbott, Eigenvalue Spectra of Random Matrices for Neural Networks, *Phys. Rev. Lett.* **97**, 188104 (2006).
- [46] J. C. Shank, M. B. Tellekamp, M. J. Wahila, S. Howard, A. S. Weidenbach, B. Zivasatienraj, L. F. Piper, and W. A. Doolittle, Scalable memdiodes exhibiting rectification and hysteresis for neuromorphic computing, *Sci. Rep.* **8**, 12935 (2018).
- [47] H. Tuller, *Ionic Conduction and Applications*, edited by S. Kasap and P. Capper (Springer International Publishing, Cham, 2017), Vol. 1, p. 1.
- [48] D. Wohlmuth, V. Epp, P. Bottke, I. Hanzu, B. Bitschnau, I. Letofsky-Papst, M. Kriechbaum, H. Amenitsch, F. Hofer, and M. Wilkening, Order vs. disorder—A huge increase in ionic conductivity of nanocrystalline LiAlO_2 embedded in an amorphous-like matrix of lithium aluminate, *J. Mater. Chem. A* **2**, 20295 (2014).
- [49] D. Wohlmuth, V. Epp, B. Stanje, A.-M. Welsch, H. Behrens, and M. Wilkening, High-energy mechanical treatment boosts ion transport in nanocrystalline $\text{Li}_2\text{B}_4\text{O}_7$, *J. Am. Ceram. Soc.* **99**, 1687 (2016).
- [50] S. Andersson and A. Wadsley, Crystallographic shear and diffusion paths in certain higher oxides of niobium, tungsten, molybdenum and titanium, *Nature* **211**, 581 (1966).
- [51] C. Nico, T. Monteiro, and M. Graça, Niobium oxides and niobates physical properties: Review and prospects, *Prog. Mater. Sci.* **80**, 1 (2016).
- [52] M. Kaviani, V. V. Afanas'ev, and A. L. Shluger, Interactions of hydrogen with amorphous hafnium oxide, *Phys. Rev. B* **95**, 075117 (2017).

- [53] See the Supplemental Material at <http://link.aps.org/supplemental/10.1103/PhysRevApplied.15.054030> for details of the first-principles modeling, the Wannierization, the variation of the Hartree potential, and the scaling analysis. The Supplemental Material includes references [64–72].
- [54] The abscissa is shifted by 1 eV to connect with the fact that the electronic structure of oxygen-deficient α -Nb₂O_{5-x} is shifted relative to the stoichiometric counterpart.
- [55] To obtain the kinetic integrals of HfO_x and α -Nb₂O_{5-x}, we have performed *ab initio* molecular-dynamic quenches and subsequent DFT calculations. Further computational details can be found in the Supplemental Material [53].
- [56] P. Basnet, D. G. Pahinkar, M. P. West, C. J. Perini, S. Graham, and E. M. Vogel, Substrate dependent resistive switching in amorphous-HfO_x memristors: An experimental and computational investigation, *J. Mater. Chem. C* **8**, 5092 (2020).
- [57] M. P. West, P. Basnet, D. G. Pahinkar, R. H. Montgomery, S. Graham, and E. M. Vogel, Impact of the thermal environment on the analog temporal response of HfO_x-based neuromorphic devices, *Appl. Phys. Lett.* **116**, 063504 (2020).
- [58] H.-G. Steinrück, C. J. Takacs, H.-K. Kim, D. G. Mackanic, B. Holladay, C. Cao, S. Narayanan, E. M. Dufresne, Y. Chushkin, B. Ruta, *et al.*, Concentration and velocity profiles in a polymeric lithium-ion battery electrolyte, *Energy Environ. Sci.* **13**, 4312 (2020).
- [59] K. Nomura and A. H. MacDonald, Quantum Transport of Massless Dirac Fermions, *Phys. Rev. Lett.* **98**, 076602 (2007).
- [60] P. Markos, Numerical analysis of the Anderson localization, [arXiv:cond-mat/0609580](https://arxiv.org/abs/cond-mat/0609580) (2006).
- [61] D. J. Thouless, Electrons in disordered systems and the theory of localization, *Phys. Rep.* **13**, 93 (1974).
- [62] L. Ceriani and P. Verme, The origins of the Gini index: Extracts from *Variabilità e Mutabilità* (1912) by Corrado Gini, *J. Econ. Inequality* **10**, 421 (2012).
- [63] S. Baranovski, *Charge Transport in Disordered Solids with Applications in Electronics* (John Wiley & Sons, Chippenhams, 2006), Vol.17.
- [64] K. Momma and F. Izumi, VESTA 3 for three-dimensional visualization of crystal, volumetric and morphology data, *J. Appl. Crystallogr.* **44**, 1272 (2011).
- [65] K. Schwarz, P. Blaha, and G. K. Madsen, Electronic structure calculations of solids using the WIEN2k package for material sciences, *Comput. Phys. Commun.* **147**, 71 (2002).
- [66] A. A. Mostofi, J. R. Yates, G. Pizzi, Y.-S. Lee, I. Souza, D. Vanderbilt, and N. Marzari, An updated version of WANNIER90: A tool for obtaining maximally-localised Wannier functions, *Comput. Phys. Commun.* **185**, 2309 (2014).
- [67] C. Nico, T. Monteiro, and M. P. Graça, Niobium oxides and niobates physical properties: Review and prospects, *Prog. Mater. Sci.* **80**, 1 (2016).
- [68] M. J. Wahila, G. Paez, C. N. Singh, A. Regoutz, S. Salis, M. J. Zuba, J. Rana, M. B. Tellekamp, J. E. Boschker, T. Markurt, J. E. N. Swallow, L. A. H. Jones, T. D. Veal, W. Yang, T.-L. Lee, F. Rodolakis, J. T. Sadowski, D. Prendergast, W.-C. Lee, W. A. Doolittle, and L. F. J. Piper, Evidence of a second-order Peierls-driven metal-insulator transition in crystalline NbO₂, *Phys. Rev. Mater.* **3**, 074602 (2019).
- [69] P. E. Blöchl, Projector augmented-wave method, *Phys. Rev. B* **50**, 17953 (1994).
- [70] G. Kresse and J. Hafner, *Ab initio* molecular dynamics for liquid metals, *Phys. Rev. B* **47**, 558 (1993).
- [71] J. P. Perdew, A. Ruzsinszky, G. I. Csonka, O. A. Vydrov, G. E. Scuseria, L. A. Constantin, X. Zhou, and K. Burke, Restoring the Density-Gradient Expansion for Exchange in Solids and Surfaces, *Phys. Rev. Lett.* **100**, 136406 (2008).
- [72] A. V. Kruckau, O. A. Vydrov, A. F. Izmaylov, and G. E. Scuseria, Influence of the exchange screening parameter on the performance of screened hybrid functionals, *J. Chem. Phys.* **125**, 224106 (2006).
- [73] P. A. Lee and A. D. Stone, Universal Conductance Fluctuations in Metals, *Phys. Rev. Lett.* **55**, 1622 (1985).
- [74] G. D. Birkhoff, Proof of the ergodic theorem, *Proc. Natl. Acad. Sci.* **17**, 656 (1931).
- [75] J. v. Neumann, Proof of the quasi-ergodic hypothesis, *Proc. Natl. Acad. Sci.* **18**, 70 (1932).
- [76] C. C. Moore, Ergodic theorem, ergodic theory, and statistical mechanics, *Proc. Natl. Acad. Sci.* **112**, 1907 (2015).